

# Oxygen-Evolving Manganese Ferrite Nanovesicles for Hypoxia-Responsive Drug Delivery and Enhanced Cancer Chemoimmunotherapy

Kuikun Yang, Guocan Yu, Rui Tian, Zijian Zhou, Hongzhang Deng,\* Ling Li, Zhen Yang, Guofeng Zhang, Dahai Liu, Jianwen Wei, Ludan Yue, Ruibing Wang,\* and Xiaoyuan Chen\*

Immunological tolerance induced by the hypoxic tumor microenvironment has been a major challenge for current immune checkpoint blockade therapies. Here, a hypoxia-responsive drug delivery nanoplatform is reported to promote chemoimmunotherapy of cancer by overcoming the hypoxia-induced immunological tolerance of tumors. The nanovesicles are assembled from manganese ferrite nanoparticles (MFNs) grafted with hypoxia-responsive amphiphilic polymers as the membrane, with doxorubicin hydrochloride (Dox) loaded in the aqueous cavities. Under hypoxic conditions in tumors, the nanovesicles can rapidly dissociate into individual MFNs to release Dox and induce decomposition of tumor endogenous H<sub>2</sub>O<sub>2</sub> for tumor hypoxia relief. As a result, the Dox-loaded nanovesicles display remarkable suppression of primary tumor growth in combination with  $\alpha$ PD-L1-mediated checkpoint blockade therapy. Furthermore, the modulation of the hypoxic tumor microenvironment facilitates a long-lasting immunological memory effect to prevent tumor recurrence and metastasis. Therefore, this hypoxia-responsive nanoplatform presents a potential strategy for both local tumor treatment and long-term protection against tumor recurrence.

## 1. Introduction

Immune checkpoint blockade (ICB) therapy has emerged as a promising therapeutic strategy for various types of cancer by modulating the immunosuppressive tumor microenvironment (TME).<sup>[1,2]</sup> In particular, monoclonal antibodies that target cytotoxic T lymphocyte associated protein 4 (CTLA-4), programmed-cell-death protein 1 (PD1) or its ligand, programmed death ligand 1 (PD-L1) have received tremendous attention and have recently been approved by the U.S. Food and Drug Administration for clinical tumor therapy.<sup>[3,4]</sup> However, ICB therapy still suffers from a low immune response rate and limited therapeutic efficacy due to the immunological tolerance of tumors.<sup>[5,6]</sup> Therefore, combination of ICB with other therapeutic modalities has been investigated to strengthen the effects of immunotherapy.<sup>[7–9]</sup>

Recent studies have revealed that chemotherapy could elicit an antitumor immune response by inducing immunogenic tumor cell death (ICD) and releasing tumor-associated antigens.<sup>[10,11]</sup> The ICD-induced immunogenicity promotes intratumoral infiltration of cytotoxic T lymphocytes (CTLs) and thus enhances tumor sensitivity toward immunotherapy. Despite the notable potential of synergistic chemoimmunotherapy, several challenges remain before their clinical translation. For instance, the non-specific distribution of chemotherapeutic agents in vivo could potentially lead to severe side effects and failure to trigger an immunogenic response. The hypoxic TME is another critical limitation for chemoimmunotherapy.<sup>[12–14]</sup> The hypoxic TME induces the recruitment of regulatory T cells (Treg), an important class of immunosuppressive cells, into the tumor and compromises the immune attack of tumor cells by CTLs. Many efforts have been undertaken to relieve hypoxia in tumors and improve the efficacy of immunotherapy.<sup>[15–17]</sup> For example, hyperbaric oxygen therapy was applied to overcome hypoxia and promote immunotherapy by introducing O<sub>2</sub> to the patients in a pressurized chamber.<sup>[18]</sup> However, this approach could lead to the overproduction of ROS in normal tissues and result in severe side

Dr. K. Yang, J. Wei, L. Yue, Prof. R. Wang  
State Key Laboratory of Quality Research in Chinese Medicine  
Institute of Chinese Medical Sciences  
University of Macau  
Avenida da Universidade, Taipa, Macau 999078, P. R. China  
E-mail: rwang@um.edu.mo

Dr. K. Yang, Dr. G. Yu, Dr. R. Tian, Dr. Z. Zhou, Dr. H. Deng, Dr. L. Li,  
Dr. Z. Yang, Dr. G. Zhang, Dr. D. Liu  
Laboratory of Molecular Imaging and Nanomedicine  
National Institute of Biomedical Imaging and Bioengineering  
National Institutes of Health Bethesda  
Bethesda, MD 20892, USA  
E-mail: hongzhang.deng@nih.gov

Prof. X. Chen  
Yong Loo Lin School of Medicine  
Faculty of Engineering  
National University of Singapore  
Singapore 119228, Singapore  
E-mail: chen.shawn@nus.edu.sg

 The ORCID identification number(s) for the author(s) of this article can be found under <https://doi.org/10.1002/adfm.202008078>.

DOI: 10.1002/adfm.202008078

effects including barotrauma and hyperoxic seizures. Although delivery vehicles loaded with perfluorocarbon, MnO<sub>2</sub> or catalase have been used to selectively relieve cancer hypoxia and improve immunotherapy efficacy, many concerns including poor biocompatibility, stability, nonspecific O<sub>2</sub> release and transitory O<sub>2</sub> generation effects still hinder clinical translation of these nanomaterials.<sup>[19–21]</sup>

To address the challenges of synergistic chemoimmunotherapy, here we report the design of hypoxia-sensitive nanovesicles to specifically deliver doxorubicin (Dox) and generate O<sub>2</sub> in tumors in order to combat their immunological tolerance. The vesicles are composed of a layer of polyethylene glycol-*b*-poly(6-(2-nitroimidazol-1-yl)hexyl methacrylate) (PEO-*b*-PNIHM)-tethered manganese ferrite nanoparticles (MFNs), and loaded with Dox in their aqueous cavities (Figure 1A). After intravenous (i.v.) injection, the Dox-loaded MFN vesicles (Dox-MVs) could passively accumulate at the tumor site by the enhanced permeability and retention (EPR) effect, followed by internalization into the tumor cells through endocytosis (Figure 1B). Thereafter, the hydrophobic 2-nitroimidazoles on the PEO-*b*-PNIHM could be converted to hydrophilic 2-aminoimidazoles via a series of selective bioreductions under the hypoxic TME.<sup>[22,23]</sup> As a result, the vesicles dissociate rapidly and release Dox specifically in the tumor to induce chemotherapy and subsequent antitumor immune response. The dissociated Dox-MVs could also release MFNs, which serve both as a contrast agent for T<sub>2</sub>-weighted magnetic resonance imaging (MRI) and an efficient catalyst for converting endogenous H<sub>2</sub>O<sub>2</sub> in the tumor to O<sub>2</sub>. By this means, the tumor-specific production of O<sub>2</sub> could significantly relieve tumor hypoxia and reverse the immunosuppressive TME, thereby promoting antitumor immune attacks induced by chemotherapy. Compared with conventional O<sub>2</sub> generators such as catalase, MnO<sub>2</sub>, and Pt nanoparticles, the MFNs-based strategy could produce O<sub>2</sub> specifically in hypoxic tumor tissues, thus leading to enhanced therapeutic efficacy and reduced side effects. With further combination with anti-PD-L1 (αPD-L1) checkpoint blockade, the hypoxia-responsive Dox-MVs demonstrate a remarkable synergistic effect to inhibit tumor growth and prevent tumor recurrence and metastasis, providing a promising nanoplatform to improve the efficacy of chemoimmunotherapy.

## 2. Results

Hydrophobic MFNs with a diameter of 11.6 ± 0.6 nm were synthesized by a thermal decomposition method reported previously (Figures S1–S3, Supporting Information).<sup>[24]</sup> 6-(2-Nitroimidazol-1-yl)hexyl methacrylate (NIHM) was synthesized and polymerized via RAFT polymerization (Figures S4–S7, Supporting Information). The resultant thiol terminated PNIHM<sub>48</sub>-*b*-PEO<sub>45</sub> (15.5 kg mol<sup>-1</sup>) was grafted onto the surface of MFNs via the thiol–ene click reaction to obtain amphiphilic building blocks (Figure S8, Supporting Information).<sup>[25]</sup> The self-assembly of block copolymer-tethered MFNs (BCP-MFNs) into MFNs vesicles (MVs) was triggered by a solvent exchange method. Dox-MVs were fabricated by assembling MFNs in an aqueous solution of Dox instead of ultrapure water. Scanning and transmission electron microscopy (SEM/TEM) images

illustrate the formation of well-defined vesicles with uniform size distributions (Figure 1C,D). The MVs are composed of a monolayer of highly densely packed MFNs in the vesicular membrane as evidenced by the high-angle annular dark-field scanning TEM and the EDS element mapping (Figure 1E,F). The size of MVs could be directly controlled from 120.9 ± 14.0 to 275.8 ± 23.9 nm by varying the graft density of BCPs on MFNs from 0.03 to 0.09 chains nm<sup>-2</sup> (Figure 1G,H; Figure S9, Supporting Information). This can be attributed to the modulation of the physical properties of the colloidal building blocks by tuning the density of BCPs on MFNs. The hydrophobic MFNs became more amphiphilic with a higher graft density of BCPs. As a result, the assemblies composed of BCP-MFNs exhibited larger diameters as the hydrophilic PEO expanded to maximize contact with water, similar to the expansion of polymersomes with a higher hydrophilic volume fraction of BCPs.<sup>[26,27]</sup> To maximize the tumor accumulation of the vehicles via the EPR effect, MVs with a size of 120.9 ± 14.0 nm were obtained and employed for the following studies.<sup>[28,29]</sup>

MVs were stable for over 30 days in a physiologically relevant environment, such as in phosphate-buffered saline (PBS) supplemented with 10% fetal bovine serum (Figure S10, Supporting Information). To evaluate the hypoxia-responsiveness of MVs in vitro, the vesicles were incubated with PBS buffer containing NADH and nitroreductases to mimic the hypoxic TME. The corresponding morphology and size changes of MVs were clearly observed by TEM and DLS analysis (Figure 1I,J). MVs swelled slightly after 30 min incubation and dissociated completely within 2 h, which can be attributed to the amphiphilicity change of BCPs in the assemblies. The hydrophobic 2-nitroimidazole groups on the side-chains of BCPs were rapidly reduced to hydrophilic 2-aminoimidazoles under hypoxic conditions, resulting in the conversion of the colloidal BCP-MFNs from amphiphilic building blocks to more hydrophilic nanoparticles (Figure S11, Supporting Information). Therefore, MVs dissociated rapidly as a result of the weakened hydrophobic-hydrophobic interactions. The hypoxia-induced dissociation of the vesicles was further verified by the release of Dox from Dox-MVs in both normoxic and hypoxic environments (Figure 1K). A small amount of Dox release (<9%) was observed from Dox-MVs after incubation under normoxic conditions for 5 h. In contrast, over 95% of Dox was released from Dox-MVs within 5 h in a hypoxic environment, indicating the hypoxia-induced dissociation of Dox-MVs and subsequent release of Dox from the vesicles.

To evaluate the catalytic effect of the assemblies, MVs were pretreated in the hypoxic environment for 2 h to induce disassembly of the vesicles, followed by incubation with a H<sub>2</sub>O<sub>2</sub> solution at an endogenous concentration (100 × 10<sup>-6</sup> M). Intact MVs were also incubated with H<sub>2</sub>O<sub>2</sub> as a control. The time-dependent consumption of H<sub>2</sub>O<sub>2</sub> and production of O<sub>2</sub> were measured by using a peroxide assay kit and an oxygen probe, respectively. The dissociated MVs initiated the decomposition of H<sub>2</sub>O<sub>2</sub> and generation of O<sub>2</sub> readily after addition into the 100 × 10<sup>-6</sup> M H<sub>2</sub>O<sub>2</sub> solution (Figure 1L,M; Figure S12, Supporting Information). More than 60% of H<sub>2</sub>O<sub>2</sub> was consumed after incubation with dissociated MVs for 60 min. However, no significant change in H<sub>2</sub>O<sub>2</sub> or O<sub>2</sub> level was observed for intact MVs, indicating that the dissociation of vesicles is a prerequisite for efficient catalytic

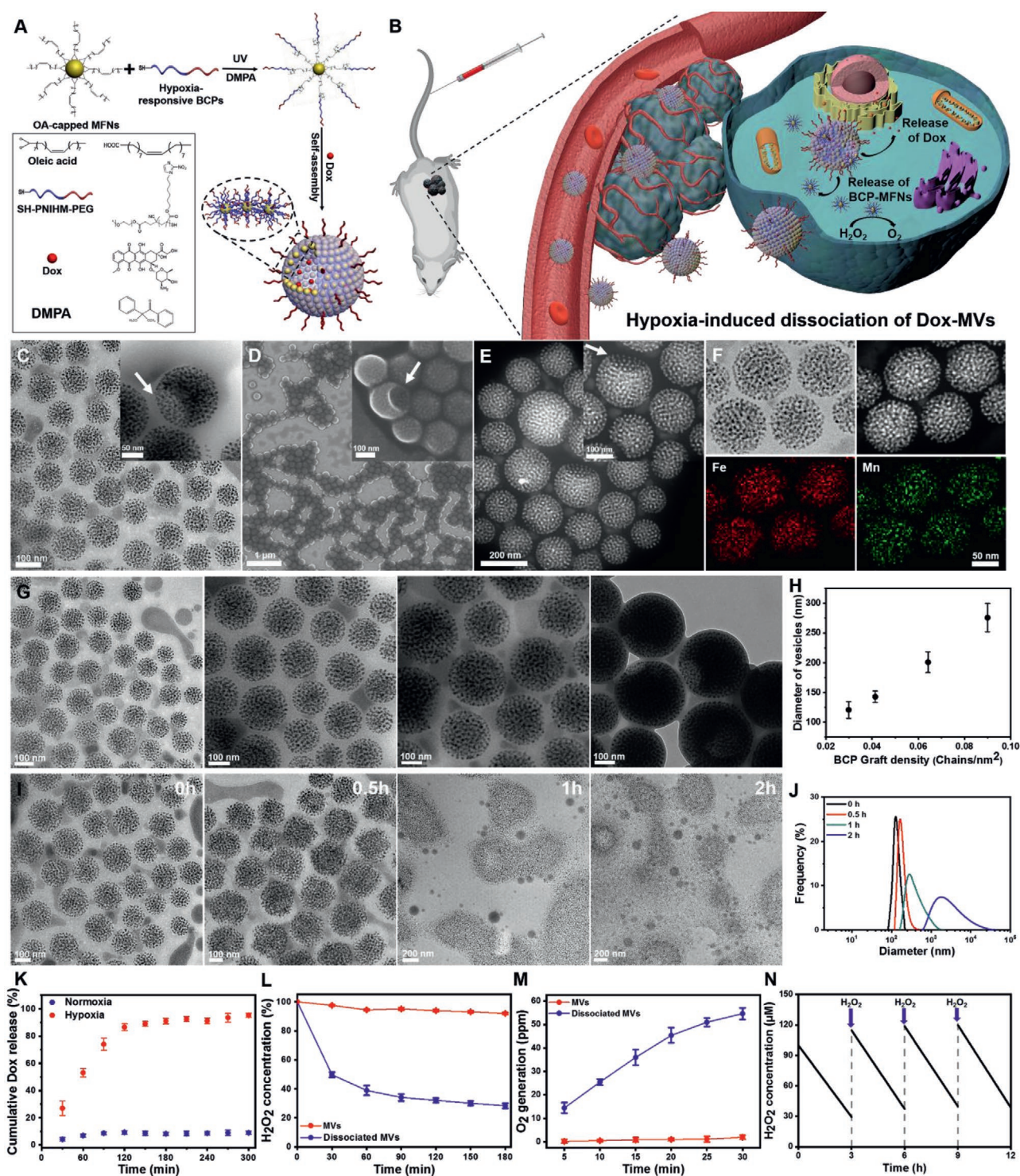


**Figure 1.** Synthesis and characterizations of vesicles composed of BCP-tethered manganese ferrite nanoparticles. A) Fabrication of Dox-MVs via cooperative assembly of BCP-grafted MFNs and B) utilization of Dox-MVs for hypoxia-responsive release of Dox and O<sub>2</sub> in tumors. C) Representative TEM, D) SEM, E) high-angle annular dark-field scanning TEM images, and F) EDS element mapping of monolayered MVs self-assembled from BCP-MFNs. The white arrows in (C–E) indicates the hollow vesicular assemblies with occasionally broken membranes. G) TEM images of MVs with various sizes and H) hydrodynamic diameters of MVs as a function of graft density of BCPs on MFNs. I) TEM images of MVs after incubation with NADH and nitroreductases for various time durations and J) the corresponding hydrodynamic diameters of MVs after incubation under hypoxic conditions. K) In vitro release of Dox from Dox-MVs after normoxia and hypoxia incubation, respectively. L) Degradation of H<sub>2</sub>O<sub>2</sub> and M) generation of O<sub>2</sub> after incubating MVs and dissociated MVs with 100 × 10<sup>-6</sup> M H<sub>2</sub>O<sub>2</sub>, respectively. N) Repetitive catalytic capability of dissociated MVs with repetitive addition of H<sub>2</sub>O<sub>2</sub>.

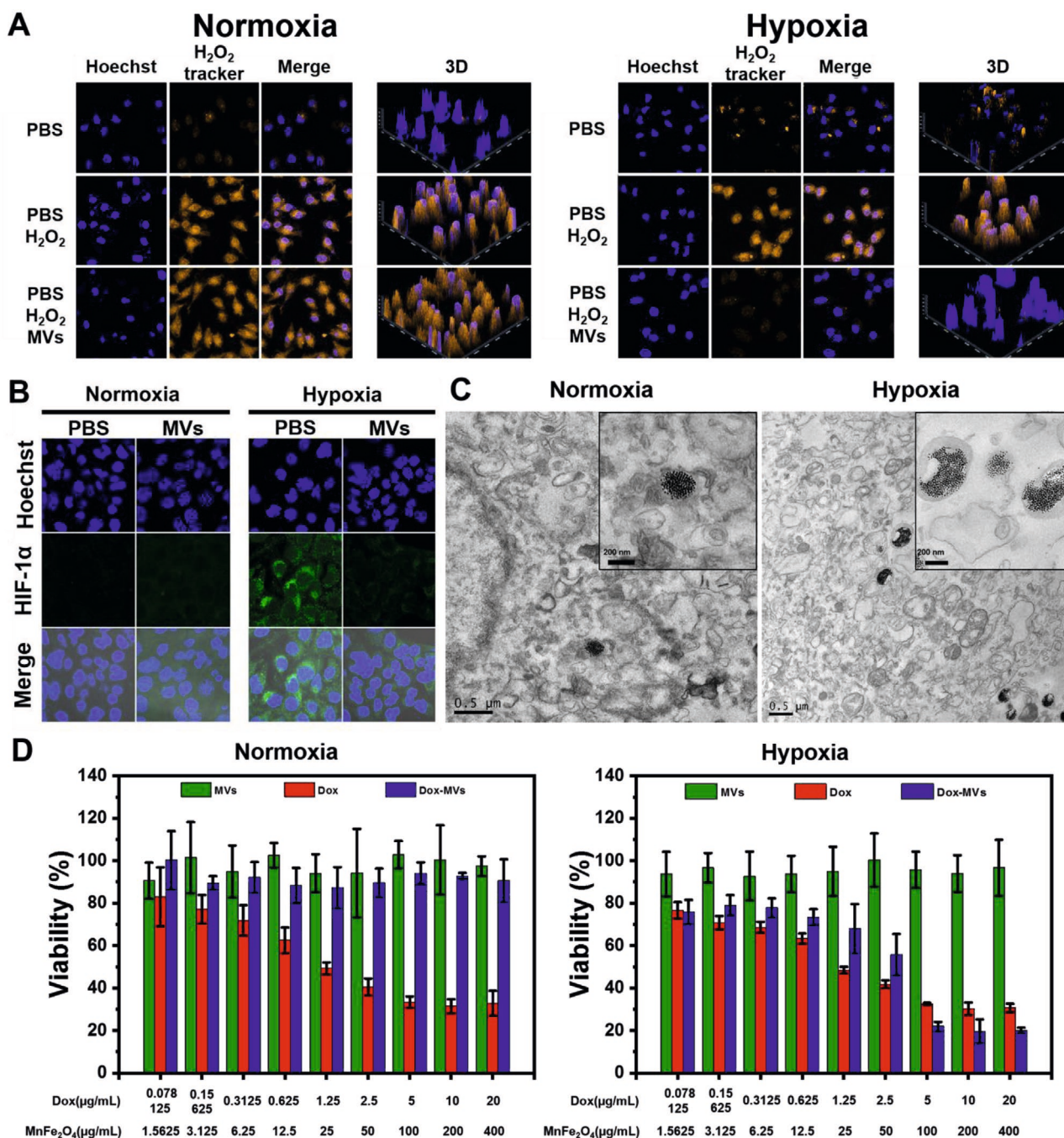


**Figure 2.** Cellular uptake, hypoxia-triggered dissociation and cytotoxicity of Dox-MVs in vitro. A) CLSM images showing the levels of intracellular H<sub>2</sub>O<sub>2</sub> in cells treated with PBS or MVs under normoxic or hypoxic conditions. B) Immunofluorescence staining showing the expression of HIF-1 $\alpha$  in 4T1 cells after incubation with PBS or MVs under normoxic and hypoxic conditions, respectively. C) TEM images of MVs treated 4T1 cells under normoxic and hypoxic conditions, respectively. D) In vitro cytotoxicity of MVs, Dox and Dox-MVs against 4T1 cells incubated under normoxic and hypoxic conditions, respectively ( $n = 5$ ). Data are presented as means  $\pm$  S.D.

decomposition of H<sub>2</sub>O<sub>2</sub> and production of O<sub>2</sub>. As MVs remain intact in a normoxic environment, the hydrophobic membrane significantly limits the accessibility of H<sub>2</sub>O<sub>2</sub> to MFNs, leading to a low catalytic activity of the vesicles. When MVs were incubated under hypoxic conditions, the vesicles dissociated into hydrophilic nanoparticles, enabling sufficient contact between H<sub>2</sub>O<sub>2</sub>

and the nanoparticles. As a result, H<sub>2</sub>O<sub>2</sub> was decomposed rapidly and a significant amount of O<sub>2</sub> was produced. Furthermore, the dissociated MVs showed continuous generation of O<sub>2</sub> after repetitive addition of H<sub>2</sub>O<sub>2</sub>, indicating the long term catalytic activity of the dissociated vesicles to continuously overcome and reverse the hypoxic TME (Figure 1N).

To further demonstrate the catalytic activity of MVs at the cellular level, the intracellular  $H_2O_2$  concentration was assessed using a fluorescent peroxide assay kit (Figure 2A). Compared with the control groups treated with PBS, strong yellow fluorescence was observed in 4T1 cells after incubation with  $100 \times 10^{-6}$  M  $H_2O_2$ . The strong fluorescence indicating a high intracellular  $H_2O_2$  level remained in cells treated with MVs and  $H_2O_2$  under normoxic conditions. Conversely, the intracellular fluorescence intensity decreased dramatically after incubation of 4T1 cells with MVs and subsequently with  $H_2O_2$  under hypoxic conditions, confirming that the hypoxia-responsive dissociation of MVs may initiate decomposition of intracellular  $H_2O_2$ . The capability of MVs to alleviate hypoxia was also investigated. As hypoxia-inducible factor 1- $\alpha$  (HIF-1 $\alpha$ ) protein is typically upregulated under hypoxic conditions, the expression of HIF-1 $\alpha$  in 4T1 tumor cells was evaluated to reveal the degree of hypoxia (Figure 2B).<sup>[30–32]</sup> In contrast to the low expression of HIF-1 $\alpha$  in 4T1 cells under normoxic conditions, a strong green fluorescence was observed in tumor cells incubated under hypoxic conditions, indicating overexpression of HIF-1 $\alpha$  induced by the hypoxic TME. However, a significant reduction in HIF-1 $\alpha$  fluorescence intensity was observed in cells treated with MVs under hypoxic conditions, indicating a dramatic alleviation of hypoxia by MVs via  $O_2$  generation. Western blot analysis further confirmed that MVs effectively overcame hypoxia in tumor cells, as evidenced by the significantly reduced signal intensity of HIF-1 $\alpha$  after incubation with MVs under hypoxic conditions (Figure S13, Supporting Information).

The hypoxia responsiveness of MVs was investigated in vitro by incubating 4T1 cells with the vesicles for 48 h under hypoxic conditions, followed by TEM observation to monitor the morphological changes of the vesicles (Figure 2C). In contrast to the intact spherical vesicles in cells under normoxic incubation, disintegrated vesicles were found in cells incubated under hypoxic conditions, confirming the hypoxia-induced dissociation of MVs.

To evaluate the chemotherapeutic effect of Dox-MVs, the cytotoxicity of free Dox, MVs and Dox-MVs on 4T1 cells in normoxic and hypoxic environments was evaluated via 3-(4,5-dimethylthiazol-2-yl)-2,5-diphenyltetrazolium bromide (MTT) assays.<sup>[33]</sup> No significant toxicity was found for cells treated with MVs at any studied concentrations ( $1.56\text{--}400 \mu\text{g mL}^{-1}$ ), indicating the excellent biocompatibility of the vesicles (Figure 2D). As expected, Dox exhibited a dose-dependent cytotoxicity against the tumor cells in both normoxic and hypoxic environments. As for 4T1 cells incubated with Dox-MVs, no obvious toxicity was observed for cells incubated under normoxic conditions. However, Dox-MVs exhibited a toxicity comparable to that of free Dox under hypoxic conditions, indicating the hypoxia-induced dissociation of Dox-MVs and subsequent release of Dox in tumor cells. To investigate the Dox-MVs induced ICD, the exposure of calreticulin (CALR) on the cell surface was evaluated as a distinct biomarker of ICD. Compared with Dox-MVs treated cells under normoxic conditions, Dox-MVs treated cells exhibited significantly higher expression of CALR under hypoxic incubation, indicating the hypoxia-triggered release of Dox and subsequent Dox-induced ICD (Figure S14, Supporting Information).

The biodistribution of Dox-MVs was evaluated in 4T1 tumor bearing Balb/c mice. MFNs were labeled with IR780 and

assembled into vesicles following the same procedure for fabrication of Dox-MVs (Figures S15 and S16, Supporting Information). The tumor-bearing mice were intravenously injected with IR780-labeled Dox-MVs and imaged at different time intervals (Figure 3A). The distribution of MVs in vivo was also evaluated for comparison (Figure S17, Supporting Information). The vesicles started to accumulate in tumors at 4 h postinjection and reached maximum accumulation at 24 h after i.v. administration as a result of the EPR effect (Figure 3B). The mice were sacrificed at 48 h postinjection and the tumors as well as major organs were collected for ex vivo imaging and quantitative analysis (Figure S18, Supporting Information). Strong fluorescence of Dox-MVs was observed in the tumor, liver and kidney of all mice, but was barely found in the heart, spleen, and lung, indicating the reticuloendothelial system-mediated clearance of Dox-MVs and renal clearance of dissociated MFNs, respectively. The accumulation of Dox-MVs in the tumor was also confirmed by  $T_2$ -weighted MR imaging (Figure 3C; Figure S19, Supporting Information). The mice injected with Dox-MVs exhibited obvious contrast in the tumor area at 24 h postinjection, compared with mice injected with PBS, confirming that intravenously injected Dox-MVs were effectively delivered into the tumor and could be used as contrast agents for imaging-guided tumor therapy.

Encouraged by the efficient catalytic activity and prolonged retention of Dox-MVs in tumors, we further evaluated the oxygenation status of the tumor after i.v. injection of the vesicles. Photoacoustic (PA) imaging was performed at different time points to evaluate the tumor vascular saturated  $O_2$  levels ( $sO_2$ ) based on the differential absorption of oxygenated and deoxygenated hemoglobin at two excitation wavelengths of 850 and 750 nm, respectively (Figure 3D).<sup>[34]</sup> Compared with the PBS and Dox treated groups, a higher level of PA signal at 850 nm appeared in the tumor of MVs or Dox-MVs treated mice at 4 h postinjection. The  $sO_2$  inside the tumor increased from  $2.7 \pm 0.7\%$  to  $17.5 \pm 4.5\%$  at 24 h after i.v. administration of Dox-MVs, which was 11.5- and 13.1-fold higher than that of the PBS and Dox treated groups, respectively (Figure 3E; Figure S20, Supporting Information). Notably, Dox-MVs treated mice exhibited increased levels of  $sO_2$  even at 48 h postinjection, indicating the extended alleviation of tumor hypoxia by Dox-MVs. To further confirm the relieved tumor hypoxia by Dox-MVs, tumor sections were collected for immunofluorescence staining of HIF-1 $\alpha$  at 24 h postinjection (Figure 3F). Compared with PBS and Dox treated groups, remarkably decreased HIF-1 $\alpha$  signals were observed for mice treated with Dox-MVs. The semi-quantitative statistical analysis of HIF-1 $\alpha$  positive areas confirmed the downregulated expression of HIF-1 $\alpha$  in the tumor after i.v. administration of Dox-MVs, indicating the efficient tumor hypoxia alleviation owing to the catalytic activity of the dissociated vesicles (Figure 3G).

Hypoxic TME is associated with immunological tolerance of tumors. Therefore, the extended relief of tumor hypoxia by Dox-MVs is anticipated to reverse the immune-suppressive TME and favor efficient tumor chemoimmunotherapy. The efficacy of Dox-MVs, in combination with PD-L1 checkpoint blockade, on tumor inhibition was evaluated with 4T1 tumor-bearing Balb/c mice. Non-catalytic BCP-tethered gold nanoparticles were assembled into Dox-loaded gold vesicles (Dox-GVs)

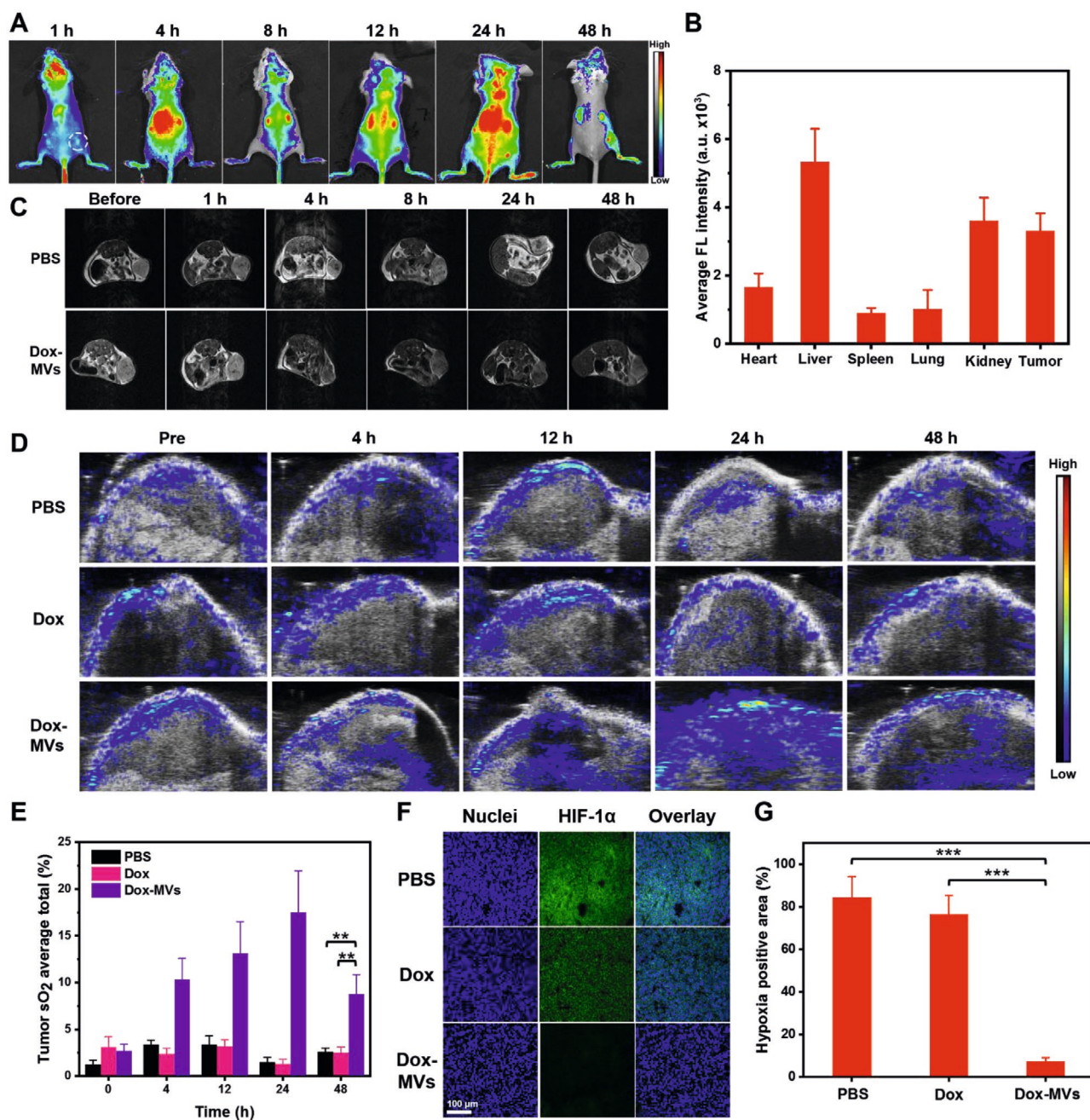


**Figure 3.** Biodistribution and hypoxia relief of Dox-MVs in 4T1 tumor-bearing mice. A) In vivo fluorescence images of 4T1 tumor-bearing Balb/c mice at different time points after intravenous injection of IR780 labeled Dox-MVs. B) Biodistribution of IR780 labeled Dox-MVs measured at 24 h post intravenous injection ( $n = 3$ ). C) In vivo  $T_2$ -weighted MR images of tumor-bearing mice at different time points before and after intravenous injection of PBS and Dox-MVs respectively. D) Representative PA images of 4T1 tumors on mice at various time points before/after intravenous injection of PBS, Dox and Dox-MVs and E) the corresponding quantification of the oxyhemoglobin saturation in tumors calculated from (D) ( $n = 3$ ). F) Immunofluorescence staining micrographs of tumor sections displaying HIF-1 $\alpha$  expression in the tumor after treatment with PBS, Dox and Dox-MVs, respectively. G) HIF-1 $\alpha$  positive areas as recorded from >10 micrographs for each group using the ImageJ software. Data are presented as means  $\pm$  S.D. (\*\*\* $p < 0.001$ , \*\* $p < 0.01$ ).

as an inert control to Dox-MVs (Figures S21–25, Supporting Information). Balb/c mice bearing 4T1 tumors were randomly divided into ten groups (five mice in each group) and were intravenously injected with 1) PBS, 2) PBS+ $\alpha$ PD-L1, 3) MVs, 4) MVs+ $\alpha$ PD-L1, 5) free Dox, 6) free Dox+ $\alpha$ PD-L1, 7) Dox-GVs, 8) Dox-GVs+ $\alpha$ PD-L1, 9) Dox-MVs, and 10) Dox-MVs+ $\alpha$ PD-L1

(equivalent Dox dose of  $1 \text{ mg kg}^{-1}$ , equivalent  $\alpha$ PD-L1 dose of  $5 \text{ mg kg}^{-1}$ ), respectively. The tumor sizes were closely monitored every two days (Figure 4A). It was found that the mice treated with PBS buffer or PBS plus  $\alpha$ PD-L1 had rapid tumor growth (Figure 4B,C). A minor delay in tumor growth was observed in the mice treated with MVs or MVs plus  $\alpha$ PD-L1, likely owing

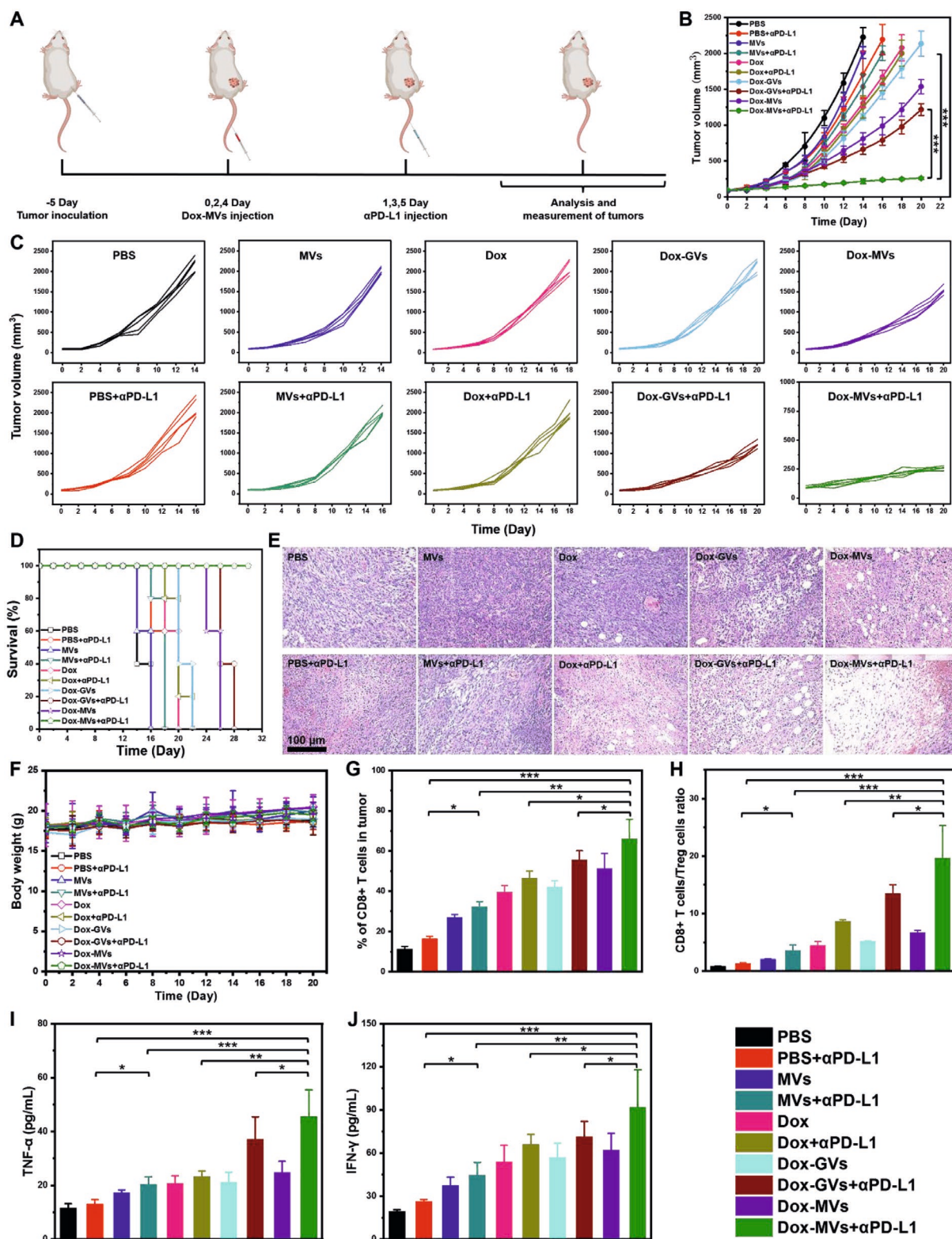


**Figure 4.** Dox-MV-mediated synergistic chemoimmunotherapy in 4T1 tumor-bearing mice. A) Schematic illustration of the treatment protocol of Dox-MV-based chemotherapy and subsequent  $\alpha$ PD-L1 combination therapy. B,C) Evolvement of tumor volumes and D) survival curves of 4T1 tumor-bearing Balb/c mice with different treatments. E) H&E staining of tumor sections collected from mice post various treatments. F) Body weight variation of 4T1 tumor-bearing Balb/c mice after various treatments. G) Proportions of tumor-infiltrating CD8<sup>+</sup> T cells (Gated on CD3<sup>+</sup>) and H) the ratio of CD8<sup>+</sup> T cells to regulatory T cells of mice post various treatments. I) TNF- $\alpha$  and J) IFN- $\gamma$  levels in the sera of mice determined on the third day post various treatments (on Day 8). Data are presented as means  $\pm$  S.D. ( $n = 5$ ,  $***p < 0.001$ ,  $**p < 0.01$ ,  $*p < 0.05$ ).

to the limited tumor-inhibitory effect of immunotherapy on the established tumors ( $\approx 100 \text{ mm}^3$ ). For tumor-bearing mice treated with free Dox or Dox plus  $\alpha\text{PD-L1}$ , the tumor growth was partially delayed in early days but a rapid growth was observed later on. This could be ascribed to the poor tumor specificity and insufficient tumor retention of free Dox at such low doses. Thanks to the tumor specific release of Dox, both Dox-GVs and Dox-MVs exhibited more significant inhibition of tumor growth and the antitumor effect was further enhanced upon combining Dox-GVs with PD-L1 blockade. However, the tumor growth was still not efficiently restrained at later time points. In contrast, Dox-MVs in combination with  $\alpha\text{PD-L1}$  showed the most significant suppression of tumor growth, suggesting that Dox-MVs could significantly promote the chemoimmunotherapy of tumors by catalytically supplying oxygen and relieving tumor hypoxia. Notably, 4T1 tumor-bearing mice treated with Dox-MVs plus  $\alpha\text{PD-L1}$  survived for over 30 days without a single death, whereas the other groups of mice showed shortened life spans of about 14–28 days (Figure 4D). In addition, both H&E and TUNEL staining of tumor tissue sections revealed that Dox-MVs plus  $\alpha\text{PD-L1}$  induced more significant apoptosis and necrosis of tumor cells in comparison with all the other groups, indicating the critical role of tumor-specific Dox delivery as well as tumor hypoxia alleviation for effective tumor chemoimmunotherapy (Figure 4E; Figure S26, Supporting Information). A negligible loss of body weight was observed for all groups of mice during the therapeutic period, indicating the biosafety of the delivery vehicles (Figure 4F). Moreover, H&E-stained images of major organs suggested no obvious histological abnormality in any of the groups, confirming the absence of obvious toxicity of our treatment (Figure S27, Supporting Information). In addition, the liver function biomarkers including alanine aminotransferase (ALT), aspartate aminotransferase (AST), alkaline phosphatase (ALP), and renal function biomarkers including blood urea nitrogen (BUN), creatinine (CREA), uric acid (UA) presented no significant difference compared with those of the control group 30 days after the i.v. injection of Dox-MVs, suggesting no significant long-term liver and renal function injury from the vesicles (Figure S28, Supporting Information).

It has been reported that the hypoxic TME impedes effective tumor immunotherapy. In particular, high infiltration of Treg in tumors induced by hypoxia has been found to correlate with poor clinical prognosis of cancer patients.<sup>[35,36]</sup> To investigate whether tumor hypoxia alleviation by our vesicles could promote immunotherapy efficacy, the tumors were collected after various treatments and the populations of different sub-groups of T-cells were analyzed by immunofluorescence staining and flow cytometry. It was found that the percentages of CD8<sup>+</sup> CTLs in tumors increased significantly after i.v. administration of Dox or Dox-loaded vesicles, and  $\alpha\text{PD-L1}$  treatment further enhanced CTL infiltration in tumors (Figure 4G; Figures S29–S32, Supporting Information). This can be attributed to the stimulated antitumor immune responses caused by Dox-induced immunogenic tumor cell death. Notably, tumors treated with Dox-MVs plus  $\alpha\text{PD-L1}$  exhibited the highest level of CTL infiltration compared to those treated with free Dox or Dox-GVs plus  $\alpha\text{PD-L1}$ , suggesting that the enhanced efficacy of immunotherapy was a result of tumor hypoxia relief. Moreover, it was also found that

mice treated with Dox-MVs plus  $\alpha\text{PD-L1}$  exhibited a moderate reduction in the population of immunosuppressive Treg within tumors when compared with other groups, implying that tumor hypoxia relief by Dox-MVs could effectively abrogate the activity of Tregs recruited into tumors (Figures S33 and S34, Supporting Information). As a result, tumors treated with Dox-MVs plus  $\alpha\text{PD-L1}$  showed the highest CD8<sup>+</sup> CTLs to Treg ratios, indicating the strongest antitumor immune response in this group, which corroborated well with the highest tumor inhibition efficacy and survival rate (Figure 4H). An increased expression of tumor necrosis factor alpha (TNF- $\alpha$ ) and interferon gamma (IFN- $\gamma$ ) was found in the sera of mice injected with Dox-MVs plus  $\alpha\text{PD-L1}$ , as compared with the other groups, further confirming that the combination of tumor hypoxia alleviation with PD-L1 checkpoint blockade contributed to the most significant anti-tumor immunity (Figure 4I,J).

The immune memory effect is crucial for long term prevention of tumor recurrence and distant metastasis.<sup>[37,38]</sup> To evaluate the immunological memory induced by Dox-MVs, Balb/c mice were subcutaneously rechallenged with 4T1 cells 28 days after the surgical resection of the primary 4T1 tumors to detect tumor recurrence (Figure 5A). For the mice treated with PBS, MVs, Dox or Dox-GVs plus  $\alpha\text{PD-L1}$ , their reinoculated tumors all grew up quickly, resulting in the death of those mice within 26 days post-tumor rechallenge (Figure 5B,C). In contrast, synergistic chemoimmunotherapy by Dox-MVs plus  $\alpha\text{PD-L1}$  significantly suppressed reinoculated tumor progression and improved the survival rate of mice. The mechanism behind this strong long-term immune memory effect of Dox-MVs plus  $\alpha\text{PD-L1}$  treatment was investigated by collecting and analyzing the spleens of mice from different groups one day before inoculation of the secondary tumor. The proportion of effector memory T cells ( $T_{EM}$ , CD3+CD8+CD62L-CD44<sup>+</sup>) crucial for immune memory protection was evaluated using flow cytometry (Figure S35, Supporting Information). In comparison with other groups, the frequency of  $T_{EM}$  significantly increased in the spleens of mice receiving Dox-MVs plus  $\alpha\text{PD-L1}$  (Figure 5D). In addition, the concentrations of TNF- $\alpha$  and IFN- $\gamma$  in the sera of mice were remarkably higher in mice treated with Dox-MVs plus  $\alpha\text{PD-L1}$  than those of the other groups, indicating the successful reactivation of strong antitumor immune responses by Dox-MVs plus  $\alpha\text{PD-L1}$  to effectively prevent recurrence of tumors (Figure 5E,F).

To further investigate the induction of immunological memory by Dox-MVs plus  $\alpha\text{PD-L1}$ , a lung metastasis tumor model was established by intravenously injecting 4T1 tumor cells into Balb/c mice. Lung metastasis inhibition was evaluated by collecting lungs from all groups of mice 14 days postinjection of tumor cells and counting the lung metastasis nodules (Figure 5G,H). The gross appearance of lung nodules revealed that Dox-MVs plus  $\alpha\text{PD-L1}$  could efficiently prevent lung metastasis when compared with the control groups. The combined treatment of Dox-MVs plus  $\alpha\text{PD-L1}$  substantially reduced the number of lung nodules to  $1.6 \pm 1.1$  per lung whereas mice treated with PBS plus  $\alpha\text{PD-L1}$ , MVs plus  $\alpha\text{PD-L1}$ , Dox plus  $\alpha\text{PD-L1}$  and Dox-GVs plus  $\alpha\text{PD-L1}$  displayed lung metastasis with  $22.2 \pm 4.4$ ,  $11.2 \pm 3.4$ ,  $8.4 \pm 2.0$ , and  $5.2 \pm 2.5$  nodules per lung respectively.

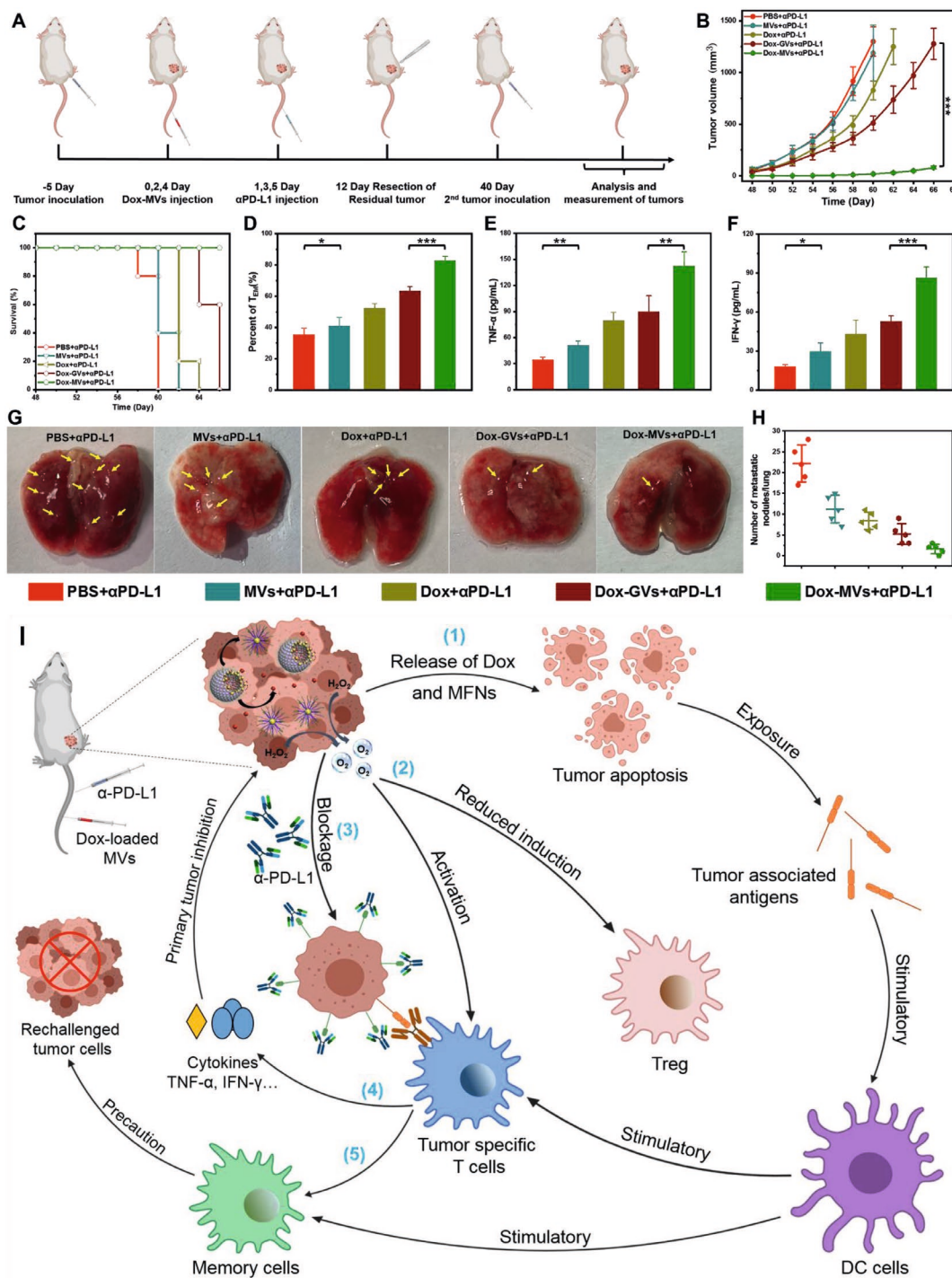


**Figure 5.** Long-term immune memory effects induced by Dox-MV-mediated chemoimmunotherapy. A) Schematic illustration of the treatment protocol with Dox-MV-based chemotherapy and subsequent  $\alpha$ PD-L1 combination therapy to inhibit cancer relapse. B) Evolution of secondary 4T1 tumor volumes after elimination of the primary tumor and C) survival curves of Balb/c mice with different treatments. D) Proportions of effector memory T cells (T<sub>EM</sub>) in the mice spleens analyzed by flow cytometry (gated on CD8<sup>+</sup>) one day before rechallenging mice with secondary tumors (on Day 39). E, F) Cytokine levels in the sera from mice isolated 7 days after mice were rechallenged with secondary tumors (on Day 47). G) Representative photographs showing the gross appearance of tumor nodules in the lungs of mice with different treatments. H) Number of lung nodules measured 14 days post i.v. injection of 4T1 tumor cells. I) Schematic illustration of the mechanism of Dox-MV-based chemoimmunotherapy to achieve systemic immune responses. 1) Hypoxia-responsive release of Dox for targeted tumor chemotherapy. 2) Hypoxia-triggered dissociation of Dox-MVs enables in situ oxygen generation and persistent hypoxia relief in tumor tissues. 3) Checkpoint blockade induces strong antitumor immune responses and the Dox-MV-mediated hypoxia relief could further promote antitumor immunities to 4) suppress primary tumor growth and 5) prevent tumor recurrence and metastasis. Data are presented as means  $\pm$  S.D. ( $n = 5$ ,  $***p < 0.001$ ,  $**p < 0.01$ ,  $*p < 0.05$ ).

### 3. Discussion

In the current study, we have developed multifunctional Dox-MVs for combined chemoimmunotherapy of cancer (Figure 5I). The nanovesicles were assembled from hypoxia responsive BCPs-tethered MFNs with Dox loaded inside the hollow cavities of vesicles as therapeutic cargoes, while MFNs could act as both a contrast agent for MRI and a catalyst to generate oxygen and relieve tumor hypoxia. Both Dox and MFNs were rapidly released in the hypoxic TME, where the former inhibits tumor growth by inducing tumor cell apoptosis and the latter promotes oxygen production in tumors to modulate the immune-suppressive environment and favor antitumor immune responses. In combination with immune checkpoint blockade by  $\alpha$ PD-L1, the hypoxia-responsive Dox-MVs could boost strong systemic antitumor immune responses as well as immunological memory to effectively suppress primary tumor growth and prevent tumor metastasis and recurrence.

Compared with other reported strategies to promote immunotherapy by reversing the hypoxic TME, our strategy of Dox-MVs plus  $\alpha$ PD-L1 based chemoimmunotherapy offers distinct advantages. First, Dox-MVs could passively accumulate in tumors via the EPR effect and dissociate into individual MFNs in response to the hypoxic TME. Subsequently, the dissociated nanoparticles could convert endogenous  $H_2O_2$  in the tumor to  $O_2$  to achieve tumor specific hypoxia relief. Therefore the immune response could be significantly boosted by modulating the immune-suppressive TME and avoiding nonspecific  $O_2$  generation. Second, MFNs demonstrated sustained catalytic ability after hypoxia-induced dissociation of Dox-MVs, indicating the potential for continuous  $O_2$  generation and tumor hypoxia relief for promoting immunotherapy efficacy. Finally, various therapeutic agents could be loaded inside the hollow cavities of the vesicles and released specifically at the tumor site due to the hypoxia-triggered dissociation of the delivery vehicles. As a result, highly effective inhibition of tumor growth could be realized by the rational combination of chemotherapy and anti-PD-L1 checkpoint blockade immunotherapy.

### 4. Conclusion

In summary, a hypoxia-responsive nanocarrier was developed for tumor-targeted delivery of Dox and oxygen. The sustained and tumor-specific hypoxia relief could modulate the immune-suppressive TME and facilitate effective inhibition of tumor growth, recurrence and metastasis when combined with anti-PD-L1 checkpoint blockade. With inherent biocompatibility, Dox-MVs may find tremendous potential in clinical translation to combat cancer, especially advanced metastatic cancer by synergistically combining chemotherapy with immunotherapy. Moreover, the long-term immunological memory induced by Dox-MVs enables potential application of the delivery platform in prevention of tumor recurrence after surgery or radiotherapy strategies.

### Supporting Information

Supporting Information is available from the Wiley Online Library or from the author.

### Acknowledgements

K.Y. and G.Y. contributed equally to this work. This work was supported by the National Science Foundation of China (Grant No. 21871301) and Research Committee at University of Macau (Grant Nos. MYRG2017-00010-ICMS and MYRG2016-00165-ICMS-QRCM). K.Y. is supported by the UM Macao Postdoctoral Fellowship. All animal experiments were performed under a National Institutes of Health Animal Care and Use Committee (NIHACUC) approved protocol.

### Conflict of Interest

The authors declare no conflict of interest.

### Keywords

chemoimmunotherapy, drug delivery, hypoxia-responsive, self-assembly

Received: December 4, 2020  
Published online: January 20, 2021

- [1] A. Ribas, J. D. Wolchok, *Science* **2018**, 359, 1350.
- [2] S. C. Wei, C. R. Duffy, J. P. Allison, *Cancer Discovery* **2018**, 8, 1069.
- [3] J. A. Seidel, A. Otsuka, K. Kabashima, *Front. Oncol.* **2018**, 8, 86.
- [4] Y. K. Chae, A. Arya, W. Iams, M. R. Cruz, S. Chandra, J. Choi, F. Giles, *J. Immunother. Cancer* **2018**, 6, 39.
- [5] P. Sharma, S. Hu-Lieskovan, J. A. Wargo, A. Ribas, *Cell* **2017**, 168, 707.
- [6] R. W. Jenkins, D. A. Barbie, K. T. Flaherty, *Br. J. Cancer* **2018**, 118, 9.
- [7] J. Galon, D. Bruni, *Nat. Rev. Drug Discovery* **2019**, 18, 197.
- [8] G. Lan, K. Ni, Z. Xu, S. S. Veroneau, Y. Song, W. Lin, *J. Am. Chem. Soc.* **2018**, 140, 5670.
- [9] Z. Chen, L. Liu, R. Liang, Z. Luo, H. He, Z. Wu, H. Tian, M. Zheng, Y. Ma, L. Cai, *ACS Nano* **2018**, 12, 8633.
- [10] C. Pfirschke, C. Engblom, S. Rickelt, V. Cortez-Retamozo, C. Garriss, F. Pucci, T. Yamazaki, V. Poirier-Colame, A. Newton, Y. Redouane, Y.-J. Lin, G. Wojtkiewicz, Y. Iwamoto, M. Mino-Kenudson, T. G. Huynh, R. O. Hynes, G. J. Freeman, G. Kroemer, L. Zitvogel, R. Weissleder, M. J. Pittet, *Immunity* **2016**, 44, 343.
- [11] R. Kuai, W. Yuan, S. Son, J. Nam, Y. Xu, Y. Fan, A. Schwendeman, J. J. Moon, *Sci. Adv.* **2018**, 4, eaao1736.
- [12] D. K.-C. Chiu, A. P.-W. Tse, I. M.-J. Xu, J. Di Cui, R. K.-H. Lai, L. L. Li, H.-Y. Koh, F. H.-C. Tsang, L. L. Wei, C.-M. Wong, I. O.-L. Ng, C. C.-L. Wong, *Nat. Commun.* **2017**, 8, 517.
- [13] Y. Li, S. P. Patel, J. Roszik, Y. Qin, *Front. Immunol.* **2018**, 9, 1591.
- [14] D. Samanta, Y. Park, X. Ni, H. Li, C. A. Zahnow, E. Gabrielson, F. Pan, G. L. Semenza, *Proc. Natl. Acad. Sci. USA* **2018**, 115, E1239.
- [15] Y. Chao, L. Xu, C. Liang, L. Feng, J. Xu, Z. Dong, L. Tian, X. Yi, K. Yang, Z. Liu, *Nat. Biomed. Eng.* **2018**, 2, 611.
- [16] H. Wang, X. Han, Z. Dong, J. Xu, J. Wang, Z. Liu, *Adv. Funct. Mater.* **2019**, 29, 1902440.
- [17] M.-Z. Zou, W.-L. Liu, F. Gao, X.-F. Bai, H.-S. Chen, X. Zeng, X.-Z. Zhang, *Adv. Mater.* **2019**, 31, 1904495.
- [18] S. M. Hatfield, J. Kjaergaard, D. Lukashev, T. H. Schreiber, B. Belikoff, R. Abbott, S. Sethumadhavan, P. Philbrook, K. Ko, R. Cannici, M. Thayer, S. Rodig, J. L. Kutok, E. K. Jackson, B. Karger, E. R. Podack, A. Ohta, M. V. Sitkovsky, *Sci. Transl. Med.* **2015**, 7, 277ra30.
- [19] G. Yang, L. Xu, Y. Chao, J. Xu, X. Sun, Y. Wu, R. Peng, Z. Liu, *Nat. Commun.* **2017**, 8, 902.

- [20] Q. Chen, J. Chen, Z. Yang, J. Xu, L. Xu, C. Liang, X. Han, Z. Liu, *Adv. Mater.* **2019**, *31*, 1802228.
- [21] Z. Meng, X. Zhou, J. Xu, X. Han, Z. Dong, H. Wang, Y. Zhang, J. She, L. Xu, C. Wang, Z. Liu, *Adv. Mater.* **2019**, *31*, 1900927.
- [22] C. Qian, J. Yu, Y. Chen, Q. Hu, X. Xiao, W. Sun, C. Wang, P. Feng, Q.-D. Shen, Z. Gu, *Adv. Mater.* **2016**, *28*, 3313.
- [23] J. Yu, Y. Zhang, Y. Ye, R. DiSanto, W. Sun, D. Ranson, F. S. Ligler, J. B. Buse, Z. Gu, *Proc. Natl. Acad. Sci. USA* **2015**, *112*, 8260.
- [24] J. Kim, H. R. Cho, H. Jeon, D. Kim, C. Song, N. Lee, S. H. Choi, T. Hyeon, *J. Am. Chem. Soc.* **2017**, *139*, 10992.
- [25] B. Liu, X. Deng, Z. Xie, Z. Cheng, P. Yang, J. Lin, *Adv. Mater.* **2017**, *29*, 1604878.
- [26] Y. Mai, A. Eisenberg, *Chem. Soc. Rev.* **2012**, *41*, 5969.
- [27] J. Leong, J. Y. Teo, V. K. Aakalu, Y. Y. Yang, H. Kong, *Adv. Healthcare Mater.* **2018**, *7*, 1701276.
- [28] J. Wang, W. Mao, L. L. Lock, J. Tang, M. Sui, W. Sun, H. Cui, D. Xu, Y. Shen, *ACS Nano* **2015**, *9*, 7195.
- [29] E. A. Sykes, J. Chen, G. Zheng, W. C. W. Chan, *ACS Nano* **2014**, *8*, 5696.
- [30] A. L. Harris, *Nat. Rev. Cancer* **2002**, *2*, 38.
- [31] H. Zhong, A. M. De Marzo, E. Laughner, M. Lim, D. A. Hilton, D. Zagzag, P. Buechler, W. B. Isaacs, G. L. Semenza, J. W. Simons, *Cancer Res.* **1999**, *59*, 5830.
- [32] P. Vaupel, A. Mayer, *Cancer Metastasis Rev.* **2007**, *26*, 225.
- [33] T. Mosmann, *J. Immunol. Methods* **1983**, *65*, 55.
- [34] M. Li, Y. Tang, J. Yao, *Photoacoustics* **2018**, *10*, 65.
- [35] S. Sakaguchi, T. Yamaguchi, T. Nomura, M. Ono, *Cell* **2008**, *133*, 775.
- [36] V. Kumar, D. I. Gabrilovich, *Immunology* **2014**, *143*, 512.
- [37] F. Pagès, A. Kirilovsky, B. Mlecnik, M. Asslaber, M. Tosolini, G. Bindea, C. Lagorce, P. Wind, F. Marliot, P. Bruneval, K. Zatloukal, Z. Trajanoski, A. Berger, W.-H. Fridman, J. Galon, *J. Clin. Oncol.* **2009**, *27*, 5944.
- [38] T. Wang, D. Wang, H. Yu, B. Feng, F. Zhou, H. Zhang, L. Zhou, S. Jiao, Y. Li, *Nat. Commun.* **2018**, *9*, 1532.